JOURNAL OF PROPULSION AND POWER
Vol. 25, No. 1, January–February 2009

Analytic Model for Single-Cycle Detonation Tube with Diverging Nozzles

Ethan A. Barbour* and Ronald K. Hanson†
Stanford University, Stanford, California 94305

DOI: 10.2514/1.35420

An analytic model for quantifying the specific impulse of a single-cycle detonation tube fitted with a diverging nozzle is developed. The model takes advantage of the fact that the detonation tube is choked, thus enabling the straight-tube and nozzle impulses to be dealt with separately. No assumptions of steady flow are needed, and the model can be applied even for nozzles that are not pressure-matched to the environment. The model is validated against ballistic-pendulum measurements. Application of the model is demonstrated by identifying optimized area ratios over a wide range of pressures. The optimized area ratio is shown to be mainly a function of the ambient/plateau pressure ratio P_∞/P_3.

Nomenclature

A	=	cross-sectional area
B	=	ratio of nozzle exit pressure to nozzle inlet pressure
C	=	combustible mixture mass
c	=	sound speed
D	=	diameter
G_1	=	geometric factor corresponding to P_3
G_2	=	geometric factor corresponding to P_∞
g	=	gravitational acceleration
h	=	mixture enthalpy per unit mass
I	=	impulse
I^{sp}	=	mixture-based specific impulse
$K_{n,1}$	=	nozzle model proportionality constant corresponding to P_3
$K_{n,2}$	=	nozzle model proportionality constant corresponding to P_∞
K_s	=	straight-tube model proportionality constant
L	=	length
M	=	Mach number
m	=	mass
$\dot{m}$	=	mass-flow rate
N	=	tamper mass
P	=	pressure
Q	=	shock factor
T	=	thrust
t	=	time
t_0	=	time from ignition to beginning of nozzle blowdown
t_1	=	time taken by the detonation wave to reach the straight-tube end
t_4	=	time starting from t_1 until nozzle thrust reaches steady state
t_5	=	time duration of steady nozzle flow
t_6	=	time between the end of steady nozzle flow to the appearance of shock at the nozzle exit
U_{CJ}	=	Chapman–Jouguet wave speed
u	=	gas velocity
V	=	volume
x	=	spatial coordinate
α	=	first factor for the straight-tube model
β	=	second factor for the straight-tube model
Δ_1	=	preblowdown impulse factor corresponding to P_3
Δ_2	=	preblowdown impulse factor corresponding to P_∞
γ	=	isentropic exponent
ε	=	ratio of exit area to straight-tube area
θ	=	temperature
ρ	=	density
τ	=	nondimensional time
Ω_1	=	blowdown impulse factor corresponding to P_3
Ω_2	=	blowdown impulse factor corresponding to P_∞

Subscripts

e	=	exit
i	=	inlet
n	=	nozzle
q	=	quiescent
s	=	straight tube
throat	=	nozzle entrance
1	=	reactant state
3	=	state of the stagnant region behind the Taylor wave
4	=	straight-tube exit state during steady flow
∞	=	ambient state

Superscripts

0	=	stagnation state
$*$	=	maximized specific impulse
$'$	=	differentiation with respect to $M_{n,e}$

Received 2 November 2007; revision received 11 September 2008; accepted for publication 11 September 2008.

*Research Assistant, Department of Mechanical Engineering, Building 660. Student Member AIAA.

†Clarence J. and Patricia R. Woodard Professor, Department of Mechanical Engineering, Building 520. Fellow AIAA.

I. Introduction

PULSED-DETONATION engines (PDEs) offer theoretical advantages over conventional constant-pressure propulsion devices as well as inherent mechanical simplicity [1]. Although most of the available chemical energy of the reactants is harnessed as work via pressure that acts on the endwall, the simple straight-tube design fails to capture a large fraction of the available energy due to the products leaving the tube at elevated pressures. The simplest way to address this concern is with a nozzle attached to the end of the straight tube. Various types of nozzles have been considered, the most common of which are diverging and converging–diverging. (Straight nozzles have also received attention [2], but in this case, the benefit arises from the tamper mass retarding blowdown of the combustion products.) Kailasanath [3] gave a review of work in PDE nozzles up to 2001.

In general, diverging and converging–diverging nozzles have been shown to improve single-cycle performance. Cambier and Tegnér [4] numerically simulated the thrust from a straight detonation tube fitted with a diverging nozzle. Both the tube and the nozzle were filled with reactive mixture. By increasing the exit area they were able to increase the impulse. Fuel-based specific impulse was also observed to increase for a sufficiently large exit area, despite the added fuel mass that resulted from the larger nozzle volumes. An optimum exit area ratio was not identified, nor was the method of choosing the range of tested area ratios discussed. Eidelman and Yang [5] also performed numerical simulations on a straight detonation tube fitted with a bell-shaped diverging nozzle. The exit/tube area ratio ε was fixed at 5. This choice was based on the pressure that acted at the endwall of the straight tube. Their design was also able to increase the impulse. The authors concluded that overexpansion played an important role in the amount of impulse attributed to the nozzle.

Morris [6] numerically simulated the effect of converging–diverging nozzles on PDE single-cycle impulse over a wide range of area ratios and ambient pressures. He showed that an optimum diverging area ratio exists for each ambient pressure. He also showed that the relative gain of an added nozzle becomes more pronounced as the ambient pressure is decreased. Owens and Hanson [7] also investigated the question of optimum area ratio by numerically simulating a PDE fitted with nozzles having different area ratios. The optimum area ratio was found to be well predicted by a steady nozzle operating with a stagnation pressure equal to the time-averaged pressure acting at the PDE endwall. The model did not, however, quantify impulse. They also established that both the diverging and converging–diverging nozzles were choked during a significant portion of the blowdown by experimentally observing expansion fans at the throat. The important conclusion was that a converging section is not needed to choke the combustion products of a PDE.

Cooper and Shepherd [8] experimentally studied the effects nozzles have on straight-tube, single-cycle impulse. The type of nozzle (converging vs converging–diverging), area ratios, and ambient pressure were tested. The nozzle contained quiescent air at ambient conditions. In all cases, the addition of a nozzle increased the specific impulse. The authors divided all cases into two broad groups: quasi-steady and unsteady. Quasi-steady blowdown was attributed to cases that had low tamper masses and thus short nozzle startup times. Unsteady blowdown corresponded to large tamper masses and thus long startup times. A simple model was developed to try to capture performance under quasi-steady operation. Complex phenomena such as transient nozzle separation were expected to be present for the unsteady cases because ambient pressures were high. Morris [9] attempted to reproduce Cooper and Shepherd's [8] measurements using a chemically reacting two-dimensional Euler-based code. Agreement was best at low ambient pressures, for which separation effects were expected to be at a minimum. Because the Euler-code was not able to capture separation, agreement at high ambient pressures was worse.

There is currently a need for a simple systematic design methodology for PDE nozzles. Although numerical techniques can be employed to identify the optimized area ratio (as was done in [6,7]), computational times make this approach undesirable. Furthermore, the resulting design would be specific to a particular straight-tube length, ambient pressure, initial pressure, fuel, oxidizer and equivalence ratio. Therefore, both a physical understanding of the transient flow through nozzles, as well as any resulting scaling laws, is required to simplify nozzle design. To address this need, a simple constant-γ model has been developed that is meant to complement the straight-tube model of Wintenberger et al. [10], later revised by Cooper and Shepherd [11]. This is done by first discussing the thrust that manifests itself in detonation-tube nozzles. Then the nozzle choke state is derived. Next, the thrust and impulse of various portions of the nozzle blowdown are quantified. The model is compared with available experimental results. Finally, the model is applied to demonstrate how an optimized exit area ratio is chosen for a particular reactant state and ambient pressure.

II. Detonation-Tube Configuration

The configuration considered is depicted in Fig. 1. The straight-tube section has a length L_s and cross-sectional area A_s, where subscript s represents a straight tube. The nozzle is conical and thus has a linearly increasing diameter. The exit area is denoted as $A_{n,e}$, where subscript n represents the nozzle and e represents the exit. The nozzle area ratio is $\varepsilon \equiv A_{n,e}/A_s$. The length of the nozzle is designated as L_n. The interface between the straight tube and the nozzle is referred to as the throat, despite the lack of a converging section. An imaginary diaphragm is placed at the throat. The initial condition consists of quiescent reactants at initial pressure P_1 and initial temperature θ_1 to the left of the diaphragm, and quiescent air at ambient pressure P_∞ and ambient temperature θ_∞ to the right of the diaphragm. Unless otherwise stated, the following baseline case is implied throughout this paper: stoichiometric C_2H_4/O_2, $P_1 = 1$ atm, $\theta_1 = \theta_\infty = 298$ K, $D_s = 50$ mm, and $L_s = 1$ m. The ignition source is located at the endwall, and direct initiation is assumed. [Deflagration-to-detonation transition (DDT) is not expected to influence the model's accuracy because [12] shows that DDT has a minimal effect on straight-tube performance.]

III. Numerical Model

In addition to the analytical model developed herein, a numerical model is employed to help understand transient flow within the nozzle, to guide nozzle design, and to quantify certain parameters used by the analytic model that could not be determined experimentally. The numerical model is described fully in [7]. The model is quasi-one-dimensional, adiabatic, and inviscid. Both endwall thrust and nozzle thrust are determined by integrating pressure over the appropriate thrust surfaces at each instant in time. Chemical mechanisms can be implemented, but a constant-γ assumption is applied for the sake of comparing with the constant-γ analytic model. Furthermore, the flow is assumed to be in chemical equilibrium. Thus, γ is not the ratio of specific heats, but rather the slope of the isentrope [with entropy evaluated at the Chapman–Jouguet (CJ) state] in $\log(P)$–$\log(\rho)$ space. (See [13] for a discussion of using frozen vs equilibrium γ.) All CJ properties (including γ) are evaluated using the STANJAN equilibrium solver [14]. Numerical simulations are initiated by imposing the constant-γ Taylor wave between the endwall and the diaphragm. (See [15] for a discussion of the Taylor wave.) This strategy makes the need to resolve the reaction zone of the detonation wave unnecessary, and so the chosen grid resolution of 0.5 mm is sufficient.

IV. Time-Varying Thrust

Because thrust and impulse are linear combinations of both the endwall and nozzle contributions, it will be convenient to break down the overall engine thrust and impulse into these two components. Figure 2 shows the time-varying thrust histories obtained via numerical simulations. The ambient pressure P_∞ was 0.01 atm. A large pressure ratio P_1/P_∞ was chosen to evade separation effects. The area ratio ε was 40. This value is close to the optimum area ratio for these conditions. The simulation was terminated when the endwall thrust reached zero. The figure is broken down into parts (Fig. 2a and Fig. 2b), the only difference being the time scale in each. Figure 2a shows the entire cycle until the endwall thrust has reached zero. Figure 2b shows detail at early times.

After ignition ($t = 0$), the detonation wave travels at CJ speed toward the diaphragm. Time t_1 corresponds to the CJ wave arriving at the diaphragm, following Wintenberger et al.'s [10] nomenclature.

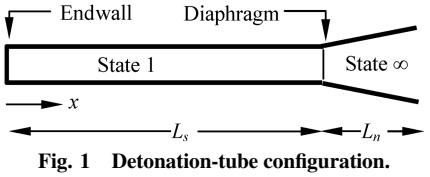

Fig. 1 Detonation-tube configuration.

The region between the Taylor wave and the endwall is labeled as state 3. P_3 persists at the thrust wall during the detonation-wave traversal of the tube and the impulse begins to accumulate. During time t_1, the endwall thrust is $(P_3 - P_1)A_s$.

After the diaphragm breaks, the endwall thrust suddenly jumps to $(P_3 - P_\infty)A_s$ because there is no longer a diaphragm acting as a negative thrust surface. (The apparent smooth rise in endwall thrust during the sudden diaphragm break, as seen in Fig. 2b, is a computational artifact.) The CJ wave transmits a shock wave into the ambient air, and thrust from the nozzle rapidly builds as this shock wave traverses the nozzle. The peak nozzle thrust corresponds to the shock wave reaching the exit of the nozzle (see Fig. 2b).

After the shock has left the nozzle, the nozzle thrust starts to decay. The dynamics of this decay are governed by passage of the Taylor wave through the nozzle, as well as the expansion waves that begin to enter the nozzle. These expansion waves later reach the endwall, at which point the endwall thrust begins its decay. Meanwhile, nozzle thrust is steady, having begun at time $t_1 + t_4$ (t_2 and t_3 were defined in Wintenberger et al.'s [10] model and so they are not repeated here). At time $t_1 + t_4 + t_5$, the nozzle begins to blow down.

Other important events include when a shock wave first appears at the nozzle exit due to overexpansion ($t_1 + t_4 + t_5 + t_6$), when the endwall reaches zero thrust, and when the shock wave that first appeared at the nozzle exit reaches the throat (the latter event happens after the endwall reaches zero thrust and so it is not shown in the figure). Several important conclusions can be drawn from this figure:

1) A nozzle that is choked [i.e., $M_{\text{throat}} = 1$ (see Fig. 2a)] need not be steady. As the pressure and burned gas velocity within the straight tube decay, the pressure and velocity at the nozzle entrance also decay, resulting in nozzle thrust decay. All the while, however, the Mach number throughout the nozzle remains steady, determined uniquely at each location by the local area ratio. The flow is in fact quasi-steady, meaning that flow parameters throughout the nozzle are changing with time, but the well-known steady nozzle equations can still be applied. That is to say, all unsteady terms appearing in the mass, momentum, and energy equations are negligible.

2) A converging section is not required for nozzle choking, as previously observed by Owens and Hanson [7]. This will be discussed in more detail in the next section.

3) The time for the transmitted shock to traverse the nozzle is very short. As the nozzle length L_n is decreased, this nozzle startup time is shortened further. In the limit of $L_n \to 0$, the importance of L_n disappears and the problem becomes self-similar in x/L_s. For all cases of realistic nozzle length and divergence angles, the transmitted shock traversal time is negligible and all cases are therefore essentially self-similar.

4) Because the nozzle is choked for nearly the entire event, the straight tube is practically unaffected by the presence of the nozzle. Only after disturbances from the environment reach the throat is the straight-tube flowfield affected by the nozzle. However, this happens so late that the endwall thrust is essentially unaffected by the presence of the nozzle. This independence of the straight tube from the nozzle will be the foundation of the current analytical model.

5) Breaking down the nozzle impulse into its components (viz., shock and Taylor wave passage t_4, steady flow t_5, nozzle blowdown t_6, and shock moving upstream), we see that each of the first three components are important. Table 1 quantifies these contributions.

These conclusions are used to lay out the strategy for developing the analytical model. First, the tamper mass residing in the nozzle will be considered to be negligible. This is true for small values of P_∞/P_1 and/or small values of L_n/L_s. The important implication is that the nozzle is instantaneously choked after the CJ wave has passed, allowing us to segregate straight-tube and nozzle flowfields from each other. Thus, the straight tube *without* a nozzle will be simulated and its time-varying exit state will be tracked to calibrate the model. Nozzle impulse will be determined by integrating thrust over $t_4 + t_5 + t_6$ (i.e., from the arrival of the CJ wave at the nozzle entrance to the appearance of a shock at the nozzle exit near the end of the cycle). Additional impulse produced by the nozzle while this shock wave moves upstream is negligible.

Before beginning the model development, we will first discuss the steady flow regime evident in Fig. 2 in more detail. This steady state can be derived analytically and will be useful later in modeling the nozzle blowdown.

V. Steady Choked State

A. Derivation

The steady thrust shown in Fig. 2 can be derived analytically by the method of characteristics. Instead of considering the nozzle configuration with a Taylor wave profile, consider a straight tube of length L with pressurized quiescent gases: $P_q > P_\infty$ and $u_q = 0$ everywhere, where q is quiescent. As before, there exists a diaphragm at $x = L$. At time zero the diaphragm breaks and gases are allowed to escape, expanding and cooling isentropically. As the gases escape they accelerate, increasing the Mach number at the exit. In fact, if the pressure differential between the exit and ambient is large enough, the exit Mach number will continue to increase until the ambient ceases to communicate with the tube flow (i.e., when the exit becomes choked). (It is interesting to note that choking, in this case, is not caused by area change, heat transfer, or friction, which are the three cases typically dealt with in introductory gasdynamic textbooks. Rather, the unsteady nature of this flow is what allows choking to take place.) We will assume that the startup time for choking is instantaneous, so that at time $t = 0^+$ the exit Mach number is unity. Figure 3 is a schematic of the characteristics in such

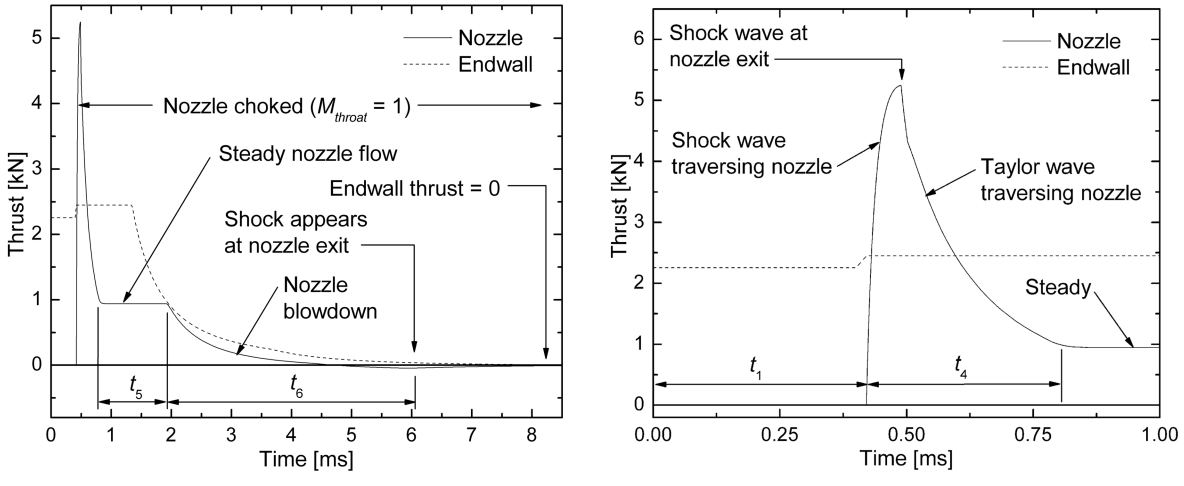

a) b)

Fig. 2 Sample histories of endwall and nozzle thrust: a) entire cycle and b) early times; $P_1 = 1$ atm, $\theta_1 = 298$ K, $\gamma = 1.14$, $P_\infty = 0.01$ atm, $\varepsilon = 40$, $L_s = 1$ m, and $L_n = 0.2$ m.

Table 1 Breakdown of the impulse; $C_2H_4 + 3O_2$, $P_1 = 1$ atm, $\theta_1 = 298$ K, $\gamma = 1.14$, $P_\infty = 0.01$ atm, $\varepsilon = 40$, $L_s = 1$ m, $L_n = 0.2$ m, and $D_s = 50$ mm

Impulse descriptor	Relevant time	Impulse, N · s	Fraction of overall impulse, %
Straight tube	Entire cycle	5.23	67
Nozzle			
Shock and Taylor wave passage	t_4	1.03	13
Steady	t_5	1.02	13
Blowdown	t_6	0.58	7
Remainder	Remainder	−0.066	<1
Overall	N/A	7.78	100

a flowfield. Also shown is the left-running characteristic moving away from the diaphragm at sound speed c_q.

Some textbooks (e.g., [16]) deal with the blowdown of a one-dimensional tube using the method of characteristics, but the exit state itself is rarely given any special attention. To proceed, we follow Thompson [17]. Recognizing that the flow is homentropic (meaning each particle experiences isentropic changes, and all particles have the same entropy), has constant area, and is without body forces, it can be shown that the Riemann variables are conserved along characteristics. In our case, we are interested in the right-moving characteristics:

$$J^+ \equiv u + \frac{2}{\gamma - 1} c = \text{constant}$$

Thus, finding the exit state is simply a matter of evaluating the Riemann invariant at a known point on the characteristic (i.e., $u = 0$ and $c = c_q$) and setting $u_e = c_e$ by virtue of the choked exit condition. As such, we obtain

$$c_e = \frac{2}{\gamma + 1} c_q$$

We now abandon the quiescent scenario and adjust the initial state to take on the Taylor wave profile. We expect to capture the same steady state at the exit because the Taylor wave is followed by its own quiescent region. In other words, although the characteristics are now much more complicated than in the wholly quiescent case, the Riemann invariant is still conserved from a stagnant region with a particular sound speed all the way to the choke point. The difference now is that the steady flow at the exit is preceded by a period of adjustment arising from the Taylor wave. The quiescent region behind the Taylor wave has traditionally been labeled as state 3. We extend this nomenclature by introducing state 4 to represent the steady flow at the exit. Thus,

$$c_4 = \frac{2}{\gamma + 1} c_3 \tag{1}$$

Using isentropic relations, we can obtain an expression for the static and stagnation pressures:

$$P_4 = \left(\frac{2}{\gamma + 1}\right)^{\frac{2\gamma}{\gamma - 1}} P_3$$

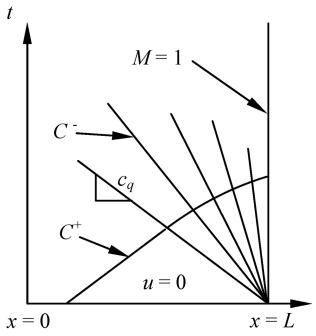

Fig. 3 Schematic of characteristics for finding the steady choked state.

$$P_4^0 = \left(\frac{2}{\gamma + 1}\right)^{\frac{\gamma}{\gamma - 1}} P_3^0$$

This is the state that persists between $t_1 + t_4 < t < t_1 + t_4 + t_5$ in Fig. 2.

Recalling that the addition of a diverging nozzle changes nothing in regard to state 4, we make the important conclusion that the stagnation pressure that exists in the nozzle during steady flow is not equal to the stagnation pressure at the endwall: $P_4^0 \neq P_3^0$. In fact, for $\gamma = 1.14$, the nozzle stagnation pressure is 57% of that of the endwall pressure. This can also be shown by considering the behavior of a fluid particle's stagnation enthalpy as the particle accelerates from near the endwall to the end of the straight tube. For adiabatic inviscid flow, the material derivative of stagnation enthalpy is given by [18]

$$\frac{Dh^0}{Dt} = \frac{1}{\rho} \frac{\partial P}{\partial t}$$

Thus, because the static pressure in the detonation tube is decreasing everywhere with time, the stagnation enthalpy of a particle must decrease as that particle is accelerated toward the exit. Likewise, the stagnation pressure must also decrease. By using the following equation of state for isentropic flow,

$$h - \frac{c^2}{\gamma - 1} = \text{constant}$$

the change in stagnation enthalpy from state 3 to state 4 can be found explicitly:

$$h_4^0 = h_3^0 - \frac{c_3^2}{\gamma + 1}$$

B. Choked-State Validation

Next, state 4 was validated experimentally. A second state was considered for the sake of comparison. This second state consisted of accelerating state 3 to the sonic condition while conserving stagnation enthalpy. This case will be referred to as choked state 3. This has been a popular approach in previous studies: for example, in [5], in which state 3 was used to design the nozzle area ratio, and in [8], in which state 3 was used to model nozzle performance. To best identify the correct state, various gasdynamic properties were calculated for both choked state 3 and state 4. These are listed in

Table 2 Gasdynamic properties of two states; $C_2H_4 + 3O_2$, $P_1 = 1$ atm, and $\theta_1 = 298$ K

	Choked state 3	State 4
h^0, MJ/kg	1.06	0.368
P, bar	7.26	4.15
θ, K	3462	3319
u, m/s	1169	1128
Mole fraction		
H_2O	0.257	0.272
OH	0.104	0.0955
CO	0.238	0.230
CO_2	0.146	0.161

Table 2 for the baseline case. STANJAN was used, and so no constant-γ assumption was required. We see that static pressure is most sensitive to the choice of model.

The validation was performed using Stanford University's detonation tube. The experimental setup is described in [19] and is repeated here for convenience. The facility consists of a stainless steel tube with a length of 1.6 m and an inner diameter of 3.81 cm. A 0.001 in. Mylar diaphragm was installed at the open end, and the tube was evacuated. A mixture of stoichiometric C_2H_4/O_2 was prepared in a separate mixing tank. Once the mixture was sufficiently mixed, the detonation tube was charged to an initial pressure P_1, which was varied between 0.4 and 2.1 atm. The initial temperature was 298 K, and the ambient pressure was maintained at 1 atm. The mixture was ignited near the closed end using a 75 mJ spark, and deflagration-to-detonation transition took place approximately 30 cm from the endwall. Three piezoelectric pressure transducers were mounted 6.83, 16, and 28 cm from the open end and covered with thermal insulation. These three measurements were extrapolated to the exit plane to obtain time-varying exit-plane static pressure. The error incurred by this extrapolation was found to be negligible compared with heat transfer effects, which are discussed in the next paragraph. Pressure at the endwall was recorded by a fourth piezoelectric transducer, also covered with thermal insulation.

Because heat transfer losses are important in a detonation tube with such a large L/D ratio [20], P_3 was slightly lower than adiabatic theory predicts. Thus, the models used to predict exit pressure were based on the measured P_3, rather than the theoretical P_3. Furthermore, because heat losses caused endwall and exit pressures to drop somewhat over time, the reported values correspond to the time-averaged pressure at the respective locations. Results are shown in Fig. 4. State 4 matches theory, whereas choked state 3 greatly overpredicts the steady exit pressure. It should also be noted that the one-dimensional theory used to determine state 4 is sufficient for capturing the exit-plane pressure, despite the flow near the exit being truly three-dimensional.

VI. Impulse Model

The model closely follows that of Wintenberger et al. [10], who broke down the impulse of a single-cycle straight detonation tube into its various components. Their model was then modified [11] to account for lowered ambient pressures. The impulse was expressed as

$$I_s = K_s(P_3 - P_\infty)\frac{V_s}{U_{CJ}} \tag{2}$$

where

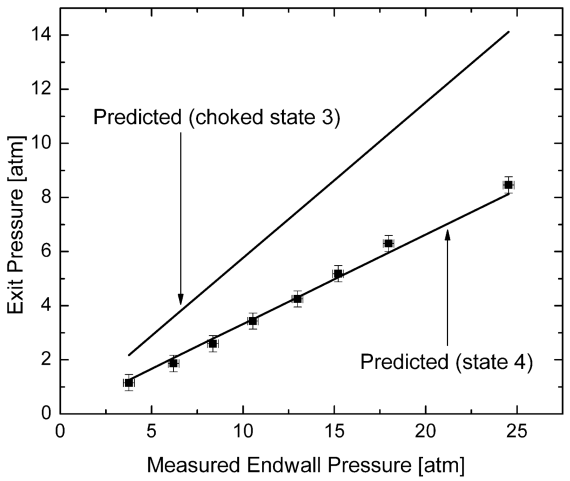

Fig. 4 Validating the state 4 model; $C_2H_4 + 3O_2$, $\theta_1 = 298$ K, $\gamma = 1.14$, and $P_\infty = 1$ atm; ■ denotes the current measurement; uncertainty bars represent the extent of pressure change due to heat transfer.

$$K_s \equiv \frac{P_3/P_1 - 1}{P_3/P_1 - P_\infty/P_1} + (\alpha + \beta)\frac{U_{CJ}}{c_3}$$

where I_s is the impulse of the straight tube in Newton seconds, and α and β are dimensionless parameters that depend on, but are very insensitive to, the state of the reactants (see [10] for further details on the definitions of α and β). Because of β's dependence on the blowdown time, it is also a function of P_∞.

A. Nozzle Thrust

To begin derivation of the nozzle impulse I_n, we first require the time-varying nozzle thrust T_n. For quasi-steady flow, we have

$$T_n = \dot{m}_n(u_{n,e} - u_{n,i}) + A_{n,e}(P_{n,e} - P_\infty) - A_{n,i}(P_{n,i} - P_\infty)$$

As before, subscript n represents the nozzle and e represents the exit. We have introduced i to represent the inlet. We next recognize that the nozzle inlet is given by the exit of the straight tube (i.e., $P_{n,i} = P_{s,e}$ and $u_{n,i} = u_{s,e}$). Because the nozzle is choked, we can obtain $P_{s,e}$ and $u_{s,e}$ by simulating the straight tube without a nozzle. It can be shown (see Appendix A) that the thrust reduces to

$$T_n(t) = A_{n,i}(P_{s,e}(t)G_1 - P_\infty G_2) \tag{3}$$

where G_1 and G_2 are geometric factors that depend on ε and γ, defined here:

$$G_1(\varepsilon,\gamma) \equiv \gamma M_{n,e}(\varepsilon M_{n,e})^{-\frac{\gamma-1}{\gamma+1}} + \varepsilon(\varepsilon M_{n,e})^{-\frac{2\gamma}{\gamma+1}} - \gamma - 1$$

$$G_2(\varepsilon) \equiv \varepsilon - 1$$

and $M_{n,e}$ is determined from ε and γ using the well-known area/Mach number relation:

$$\varepsilon = \frac{1}{M_{n,e}}\left[\frac{1 + [(\gamma-1)/2]M_{n,e}^2}{(\gamma+1)/2}\right]^{\frac{\gamma+1}{2(\gamma-1)}} \tag{4}$$

Figure 5 shows G_1 and G_2. Two values of γ are shown, where $\gamma = 1.14$ corresponds to equilibrium chemistry and $\gamma = 1.24$ corresponds to frozen chemistry, both for $C_2H_4 + 3O_2$.

B. Impulse from Taylor Wave and Steady Flow

The nozzle impulse is now found by integrating Eq. (3) in time. For times spanning t_4 (Taylor wave passage) and t_5 (steady flow) (see Fig. 2), the integration is straightforward:

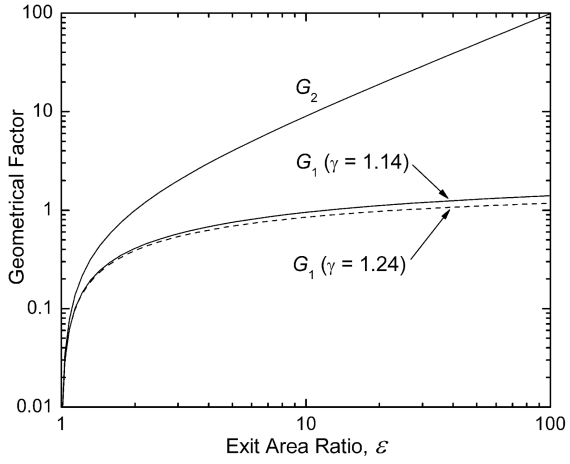

Fig. 5 Geometric factors required to calculate nozzle thrust.

$$I_n = \int_{t_1}^{t_1+t_4+t_5} T_n \mathrm{d}t$$

$$I_n = \frac{A_{n,i}L_s}{c_3}\left(P_3 G_1 \int_{\tau_1}^{\tau_1+\tau_4+\tau_5} \frac{P_{s,e}(\tau)}{P_3}\mathrm{d}\tau - P_\infty G_2 \int_{\tau_1}^{\tau_1+\tau_4+\tau_5} \mathrm{d}\tau\right)$$

$$I_n = \frac{V_s}{c_3}(P_3 G_1 \Delta_1 - P_\infty G_2 \Delta_2)$$

where

$$\Delta_1 \equiv \int_{\tau_1}^{\tau_1+\tau_4+\tau_5} \frac{P_{s,e}(\tau)}{P_3}\mathrm{d}\tau \qquad \Delta_2 \equiv \int_{\tau_1}^{\tau_1+\tau_4+\tau_5} \mathrm{d}\tau = \tau_4 + \tau_5$$

We have introduced c_3 and L_s due to the nondimensionalizing of time ($\tau \equiv tc_3/L_s$), following [10]. V_s is the volume of the straight tube. Because the flow is self-similar, Δ_1 and Δ_2 are completely independent of geometry and ambient pressure and depend only on the state of the reactants. The exit pressure of a straight tube without a nozzle was monitored for various mixtures to obtain Δ_1 and Δ_2. Results are shown in Table 3. We notice that these quantities depend weakly on the initial state. Recall that α and β also depend weakly on the initial state.

C. Impulse from Nozzle Blowdown

For sufficiently large P_∞/P_1, the impulse produced from nozzle blowdown is negligible. For these cases, this section of the paper can be ignored. For sufficiently small P_∞/P_1, however, the nozzle blowdown can contribute on the order of 10% of the overall tube and nozzle impulse (see Table 1). As in the previous section, we will identify two more nondimensional factors, Ω_1 and Ω_2, which will be used to evaluate the impulse. Like Δ_1 and Δ_2, Ω_1 and Ω_2 will depend on the initial reactant state. Unlike Δ_1 and Δ_2, however, Ω_1 and Ω_2 will also depend on P_∞ and ε. This is analogous to the way β depends on P_∞ in the straight-tube model. In both models, the impulse increases with blowdown time and blowdown time strongly depend on ambient pressure.

One option for finding Ω_1 and Ω_2 as functions of P_∞ and ε is to run simulations for all anticipated cases. However, a much simpler approach is possible if the following simplification is made. We assume that by the time nozzle blowdown begins, the contents of the straight tube are spatially uniform. This reduces the problem to that of an isentropic constant-volume blowdown with an initial state equal to state 4. The pressure is given by (see Appendix B)

$$\frac{P_{s,e}(t)}{P_4} = \left(1 + \frac{\gamma-1}{2}\frac{c_4(t-t_0)}{L_s}\right)^{-\frac{2\gamma}{\gamma-1}} \tag{5}$$

where $t_0 = t_1 + t_4 + t_5$. Figure 6 compares the true straight-tube exit pressure with that predicted by Eq. (5) for the baseline case with $P_\infty = 0.01$ atm. Agreement is more than adequate to capture the desired impulse.

Table 3 Preblowdown impulse factors taken from simulations of a straight tube without a nozzle (i.e., limit as $N/C \to 0$); $\theta_1 = 298$ K

Reactants	P_1, atm	P_3, atm	γ^b	Δ_1	Δ_2
$H_2 + \frac{1}{2}O_2$	1.0	7.12	1.13	0.84	1.80
$H_2 + \frac{1}{2}$air[a]	1.0	5.93	1.16	0.81	1.79
$C_2H_4 + 3O_2$	1.0	12.3	1.14	0.84	1.80
$C_2H_4 + 3O_2$	2.0	25.3	1.14	0.84	1.80
$C_2H_4 + 3O_2$	3.0	38.4	1.15	0.85	1.81
$C_2H_4 + 3$air[a]	1.0	6.91	1.16	0.87	1.92
JP10 + $14O_2$	1.0	14.5	1.14	0.90	1.92
JP10 + $14O_2$	2.0	29.7	1.14	0.85	1.81
JP10 + $14O_2$	3.0	45.1	1.14	0.84	1.80
JP10 + 14air[a]	1.0	7.01	1.16	0.88	1.93

[a]Air represents $O_2 + 3.76N_2$.
[b]All γ correspond to chemical equilibrium evaluated at the CJ state.

The thrust is obtained from Eq. (3) and then integrated from t_0 to $t_0 + t_6$. The duration t_6 is said to have elapsed when a shock wave appears at the nozzle exit, which occurs when

$$P_{n,e} = P_\infty \frac{\gamma+1}{2\gamma M_{n,e}^2 - \gamma + 1}$$

It is straightforward to show that t_6 is

$$t_6 = \frac{2}{\gamma-1}\frac{L_s}{c_4}\left[\left(Q\frac{P_\infty}{P_3}\right)^{-\frac{\gamma-1}{2\gamma}} - 1\right] \tag{6}$$

where

$$Q(\varepsilon,\gamma) \equiv \frac{P_3}{P_4}\frac{P_{n,i}}{P_{n,e}}\frac{P_{n,e}}{P_\infty} = \left(\frac{\gamma+1}{2}\right)^{\frac{2\gamma}{\gamma-1}}(\varepsilon M_{ne})^{\frac{2\gamma}{\gamma+1}}\frac{\gamma+1}{2\gamma M_{ne}^2 - \gamma + 1}$$

and where the ratio of nozzle exit to inlet pressures (denoted by B) was used:

$$B \equiv \frac{P_{n,e}}{P_{n,i}} = \left(\frac{\frac{\gamma+1}{2}}{1+\frac{\gamma-1}{2}M_{n,e}^2}\right)^{\frac{\gamma}{\gamma-1}} = (\varepsilon M_{n,e})^{-\frac{2\gamma}{\gamma+1}} \tag{7}$$

The parameter Q is called the shock factor and is plotted in Fig. 7.

The nozzle thrust can now be integrated to obtain blowdown impulse:

$$I_n = \int_{t_1+t_4+t_5}^{t_1+t_4+t_5+t_6} T_n \mathrm{d}t \qquad I_n = \frac{V_s}{c_3}(P_3 G_1 \Omega_1 - P_\infty G_2 \Omega_2) \tag{8}$$

where Ω_1 and Ω_2 have the analytic expressions

$$\Omega_1 \equiv \left(\frac{2}{\gamma+1}\right)^{\frac{2\gamma}{\gamma-1}}\left[1 - \left(Q\frac{P_\infty}{P_3}\right)^{\frac{\gamma+1}{2\gamma}}\right] \tag{9}$$

$$\Omega_2 \equiv \frac{\gamma+1}{\gamma-1}\left[\left(Q\frac{P_\infty}{P_3}\right)^{-\frac{\gamma-1}{2\gamma}} - 1\right] \tag{10}$$

(see Appendix C for details).

D. Overall Impulse

The expression for the nozzle impulse is

$$I_n = (P_3 K_{n,1} - P_\infty K_{n,2})\frac{V_s}{U_{\mathrm{CJ}}} \tag{11}$$

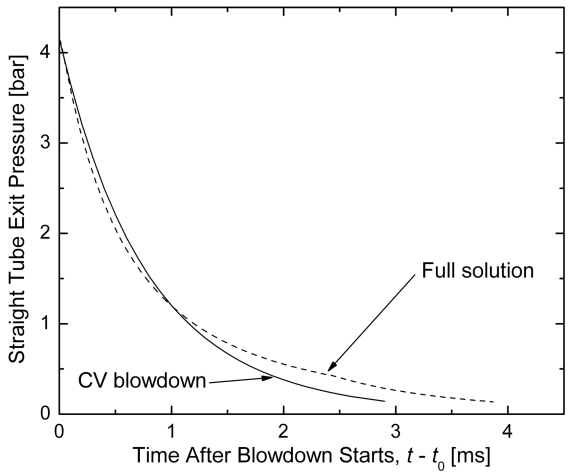

Fig. 6 Decay of straight-tube exit pressure, comparing the full solution with constant-volume (CV) blowdown [Eq. (5)]; both solutions are terminated when the pressure is such that a shock wave would appear at the nozzle exit for $\varepsilon = 40$; $C_2H_4 + 3O_2$, $P_1 = 1$ atm, $\theta_1 = 298$ K, $P_\infty = 0.01$ atm, $\gamma = 1.14$, $P_4 = 4.15$ bar, $c_4 = 1128$ m/s, and $L_s = 1$ m.

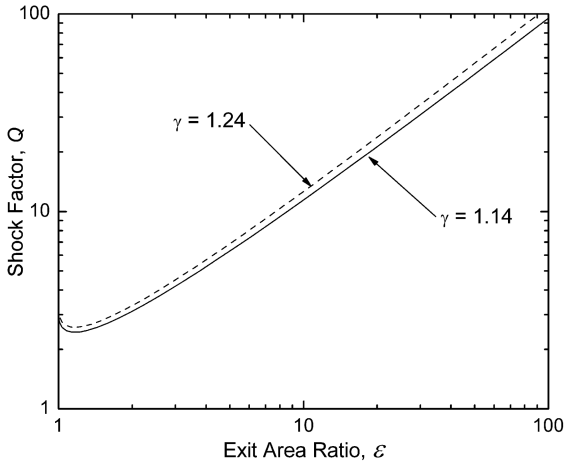

Fig. 7 Shock factor Q.

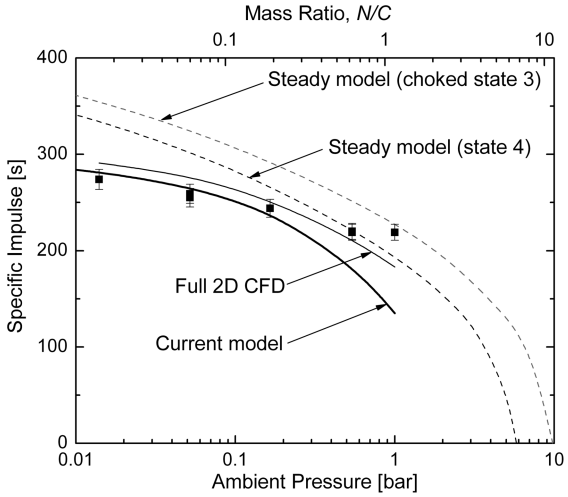

Fig. 8 Comparison of experimental data with models; ■ and steady model using choked state 3 are from [8] and the full 2-D CFD model is from [9]; $C_2H_4 + 3O_2$, $P_1 = 80$ kPa, $\theta_1 = 298$ K, $\gamma = 1.14$, and $\varepsilon = 6.5$.

where

$$K_{n,1} \equiv \frac{U_{\mathrm{CJ}}}{c_3} G_1(\Delta_1 + \Omega_1) \qquad K_{n,2} \equiv \frac{U_{\mathrm{CJ}}}{c_3} G_2(\Delta_2 + \Omega_2)$$

If the impulse from nozzle blowdown is ignored, we set $\Omega_1 = \Omega_2 = 0$. Equation (11) is analogous to Eq. (2), derived for the straight tube without a nozzle. Note that both I_n and I_s are proportional to the straight-tube volume and inversely proportional to the CJ wave speed. Both impulses are also proportional to a pressure difference, modified by constants; I_s depends directly on $K_s(P_3 - P_\infty)$, whereas I_n involves constants that cannot be factored out because the pressure difference across the nozzle wall changes as we move from the throat to the nozzle exit.

The overall impulse and specific impulse are given, respectively, by

$$I = I_s + I_n \qquad I^{\mathrm{sp}} = \frac{I}{V_s \rho_1 g}$$

These relations can now be used to find the specific impulse for any straight-tube geometry, nozzle area ratio, reactant state, and ambient pressure, as long as the tamper mass does not significantly impede nozzle startup. Table 3 is used to determine Δ_1 and Δ_2, Eqs. (9) and (10) are used to determine Ω_1 and Ω_2, and Eq. (11) is used to determine I_n. I_s is calculated entirely using the Wintenberger–Cooper model, repeated here as Eq. (2).

VII. Model Validation

There is a scarcity of experimental data available in the literature for a single-cycle impulse from detonation tubes with nozzles. Cooper and Shepherd [8] performed a comprehensive study in which they measured impulse using a ballistic pendulum over a wide range of ambient pressures. The initial mixture was stoichiometric C_2H_4/O_2 at 80 kPa and 298 K. Several nozzles were tested; the results from one of them (diverging nozzle, $\varepsilon = 6.5$) are presented here. Figure 8 shows the experimental measurements along with several models. The top axis shows the ratio of tamper mass to the reactant mass (N/C), which, for these conditions, is related to ambient pressure (in bar) by $N/C = 1.153 P_\infty$.

The two dotted lines represent model results that follow Cooper and Shepherd's [8] strategy. The model assumes that the nozzle is steady and pressure-matched to the ambient. This leads to the following expression for specific impulse:

$$I^{\mathrm{sp}} = \frac{u_{n,e}}{g}$$

Thus, by specifying the nozzle area ratio and the inlet state, we can determine the outlet state and thereby obtain I^{sp}. The question remains as to which inlet state to use. Cooper and Shepherd [8] chose to use the state that corresponded to choked flow with the same stagnation enthalpy as at state 3. This state has been labeled as choked state 3 in an earlier section. The second dotted line is the same model, but uses state 4 as the nozzle's inlet state. This correction enables the steady-state model to perform better, but it still greatly overpredicts I^{sp} at low P_∞; this is due to the pressure-matched assumption. An actual steady nozzle operating under these conditions would be underexpanded, resulting in a lower predicted I^{sp}.

The current model is shown as a dark solid line. Agreement is best at low ambient pressures. As N/C approaches the order of unity, the current model fails to predict I^{sp}. There are two reasons for this: First, nozzle startup time is prolonged, which results in significant impulse generated as the transmitted shock passes through the nozzle. Second, flow separation in the nozzle tends to increase impulse above that predicted when separation is ignored. This is because the pressure is not allowed to stay subatmospheric downstream of the separation point. (See [8,21] for further discussion of separation.) It should be pointed out that N/C is proportional to both P_∞/P_1 and L_n/L_s. Although the current model diverges from the available data at an ambient pressure of $P_\infty \sim 0.2$ bar ($P_\infty/P_1 \sim 0.25$), agreement would likely improve if L_n/L_s were decreased. The so-called Gurney model is sometimes employed to deal with the tamper mass [22]. This adjustment was made, but it was found that the Gurney model increases the predicted I^{sp} too much. This is discussed further in Sec. IX.

The increased impulse due to delayed startup time can be accounted for by performing a full computational fluid dynamics (CFD) computation. This computation was performed by Morris [9] and is included in Fig. 8. The CFD model approaches the experimental data at high ambient pressure yet still falls short due to the unmodeled flow separation. At low ambient pressure the CFD model overpredicts the data. This is likely due to losses such as heat transfer and friction. The current model, on the other hand, is able to capture these effects because it relies on the parameter β, which was obtained experimentally from a tube without a nozzle; β therefore inherently subsumes nonideal effects.

Despite disagreements between models and experiment, it should be kept in mind that a given nozzle should be intended for a particular ambient pressure, at least for cruise applications. The current model can be used to infer the best ambient pressure for the nozzle and initial conditions of Fig. 8 (see Sec. VIII). This leads to an ideal ambient pressure of $P_\infty = 0.1$ bar, well within the range of agreement with Cooper and Shepherd's [8] experimental data and Morris's [9] CFD calculations.

VIII. Nozzle Design

The current model can now be used to design diverging nozzles for PDEs with the optimal area ratio for a given reactant state and ambient pressure. Because I_s does not depend on ε, only I_n needs to be considered in this optimization procedure. After choosing the reactant and ambient states, the most straightforward and accurate way to proceed is to vary ε in Eq. (11) until I_n is maximized. This gives the optimized area ratio, denoted as ε^*, and its corresponding nozzle impulse. The straight tube impulse is then added to get the overall impulse. The result is normalized by reactant weight to obtain the specific impulse. The results are plotted in Fig. 9 for the baseline case. Also included is the specific impulse from a straight tube. This shows the level of increase in specific impulse by the addition of an optimized diverging nozzle. The optimized area ratio is also shown as a solid line. (An additional dotted line, also labeled as the optimized area ratio, corresponds to a simplified model and will be discussed next.) As required by the model, instantaneous nozzle startup is assumed and separation is ignored.

A slightly different approach to identifying the optimized area ratio ε^* provides some insight into its dependence on pressure. Because Eq. (11) is a function of ε, it can (in principle) be differentiated with respect to ε, set to zero, and solved to find ε^*. However, Eq. (11) cannot be written explicitly in terms of ε. Therefore, we instead differentiate with respect to $M_{n,e}$, find $M^*_{n,e}$, and then use Eq. (4) to extract ε^*. All differentiations with respect to $M_{n,e}$ are denoted with a prime. We obtain

$$I'_n = (P_3 K'_{n,1} - P_\infty K'_{n,2}) \frac{V_s}{U_{\mathrm{CJ}}} = 0$$

which reduces to

$$P_3(G'_1(\Delta_1 + \Omega_1) + G_1(\Delta_1 + \Omega_1)') - P_\infty(G'_2(\Delta_2 + \Omega_2) + G_2(\Delta_2 + \Omega_2)') = 0$$

In the interest of obtaining an analytical solution, we neglect the second and fourth terms:

$$\frac{G'_1}{G'_2} = \frac{P_\infty}{P_3}\frac{\Delta_2 + \Omega_2}{\Delta_1 + \Omega_1} \tag{12}$$

The induced error caused by this step is less than 1% in overall specific impulse. It can be shown (see Appendix D) that G'_1/G'_2 is given by

$$\frac{G'_1}{G'_2} = (\varepsilon^* M^*_{n,e})^{-\frac{2\gamma}{\gamma+1}} \tag{13}$$

Combining Eqs. (12) and (13) leads to

$$(\varepsilon^* M^*_{n,e})^{-\frac{2\gamma}{\gamma+1}} = \frac{P_\infty}{P_3}\frac{\Delta_2 + \Omega_2}{\Delta_1 + \Omega_1}$$

The left and right sides are functions of $M_{n,e}$, and so the solution is found using a simple iterative solution-finder (e.g., Excel's Goal Seek). We next find ε^* immediately from $M^*_{n,e}$. Figure 9 shows the optimized area ratio obtained by this method (labeled simplified) for the baseline case. Notice that there is some disagreement between this ε^* and that obtained by manually tuning Eq. (11). When translated to I^{sp}, however, the discrepancy is less than 1%. Knowing that Δ_1 and Δ_2 are insensitive to the initial mixture, we may expect the same for Ω_1 and Ω_1, in which case, ε^* depends only on P_∞/P_3 (recall that Ω_1 and Ω_2 depend on P_∞/P_3). Figure 10 shows ε^* for various fuels and oxidizers plotted against P_∞/P_1, the important ambient-to-fill pressure ratio. Figure 11 shows the same data plotted against P_∞/P_3, the ambient-to-plateau pressure ratio.

Indeed, we find that by plotting ε^* against P_∞/P_3 instead of P_∞/P_1, the data come close to collapsing onto a single line. The reason for this dependence of I^{sp} and ε^* on P_∞/P_3 is that P_3 and P_∞ determine how much impulse can be obtained by the products, regardless of what reactant state was used to produce the products. A second-order least-squares fit to these data yields a convenient design tool for sizing the optimized exit area ratio:

$$\ell_n(\varepsilon^*) = a_1\left[\ell_n\left(\frac{P_\infty}{P_3}\right)\right]^2 + a_2\,\ell_n\left(\frac{P_\infty}{P_3}\right) + a_3 \tag{14}$$

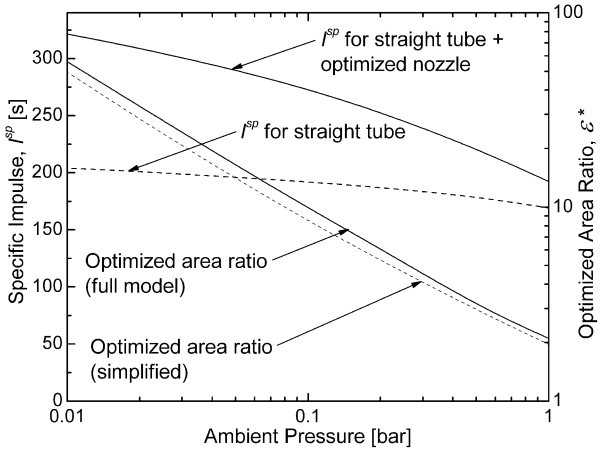

Fig. 9 Optimized nozzle design vs ambient pressure; $C_2H_4 + 3O_2$, $P_1 = 1$ atm, $\theta_1 = 298$ K, and $\gamma = 1.14$.

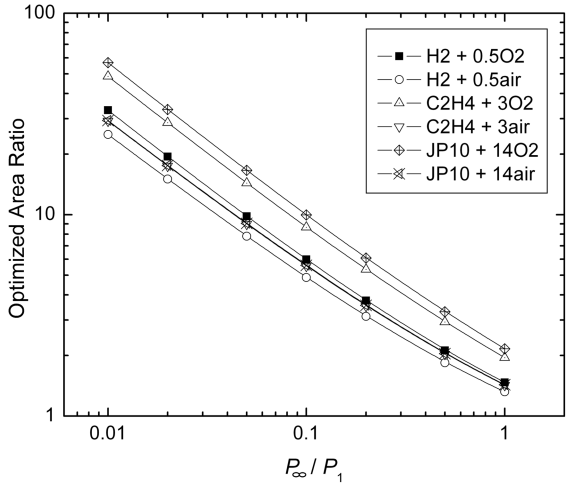

Fig. 10 Predicted optimized area ratio vs ambient/fill pressure ratio; $P_1 = 1$ atm and $\theta_1 = 298$ K.

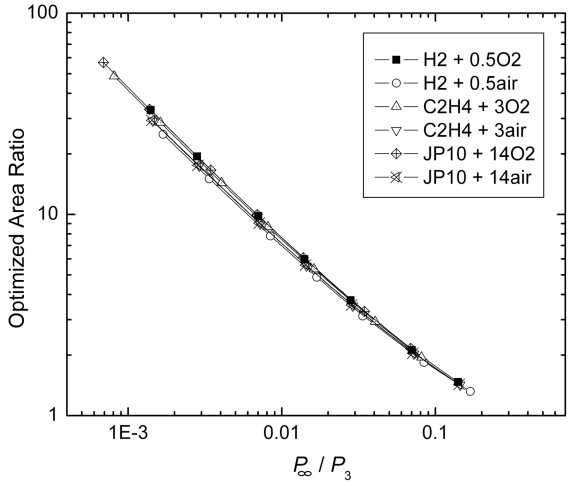

Fig. 11 Predicted optimized area ratio vs ambient/plateau pressure ratio; $P_1 = 1$ atm and $\theta_1 = 298$ K.

where $a_1 = 0.0281$, $a_2 = -0.431$, and $a_3 = -0.596$. Owens and Hanson [7] numerically simulated stoichiometric C_2H_4/O_2 with $P_1 = 1$ atm and found that the specific impulse was optimized for $\varepsilon^* = 1.8$. This agrees well with Eq. (14), which predicts $\varepsilon^* = 1.9$. We remind the reader, however, that the most accurate results are obtained by manually tuning ε^* via Eq. (11) to maximize I_n, rather than Eq. (14), which is only an approximation.

IX. Model Limitations

Although the model developed here performs well under certain conditions, there are still important limitations that need to be addressed in the future. The limitations imposed by a large tamper mass have previously been dealt with using a Gurney model [22,23]. This technique was applied to the current model to improve our I^{sp} predictions at higher values of N/C. As expected, the Gurney model increased the predicted specific impulse. However, the increase in I^{sp} was too great, leading to an overprediction of performance. This is likely due to the fact that the standard Gurney model assumes the tamper mass to be rigid. Thus, improvements could be made to the current model by applying a pseudo-Gurney model that takes into account compressibility of the tamper mass.

The current model addresses purely diverging nozzles. Because adding a converging section would affect the impulse generated by the endwall via reflected compression waves, it is not possible to incorporate a converging section into the current model. However, a model that addresses only diverging nozzles is still highly valuable in light of what other authors [7,8] have found: namely, that adding a converging section to a nozzle reduces the specific impulse. This is a result of the negative thrust produced by the converging section, as well as enhanced heat transfer from the prolonged blowdown times. However, under certain conditions it may be beneficial to have a converging section. For example, a converging section would make it possible to achieve a fill pressure that is higher than the ambient pressure ($P_1 > P_\infty$) under a dynamic filling scheme. In cases in which a converging section is necessary, the negative effects it introduces could be minimized by making the throat area only slightly smaller than the straight-tube area. This recommendation is based on the work by Cooper and Shepherd [8], who found that I^{sp} increased as the throat area increased. Additional work needs to be performed to ascertain the largest throat area that still chokes the flow during engine filling.

Finally, the single-cycle nature of the current model should be addressed. PDEs operate on a multicycle basis, and so the current model is a good predictor of performance if we assume that there is no interaction between cycles. This will depend on many factors, including engine design and the amount of purging done when removing products. In any case, the current single-cycle model is a good place to start when determining the feasibility of nozzles during multicycle PDE design.

X. Conclusions

This paper discussed several models for predicting specific impulse from a single-cycle detonation tube fitted with a diverging nozzle. When compared with available experimental data, we found that the model proposed herein predicts the specific impulse best, because it makes no assumptions about steady flow or pressure matching. However, the model must be restricted to conditions having low tamper masses. CFD models also perform well, but at the expense of long computational times.

The model was then used to demonstrate how an area ratio could be chosen for a given fuel, oxidizer, initial pressure, and ambient pressure. The optimized area ratio is almost entirely dependent on the ambient/plateau pressure ratio.

The exit state of a detonation tube was also briefly discussed. The important conclusion was that the stagnation pressure inside the nozzle is lower than the stagnation pressure at the endwall.

Appendix A: Deriving Equation (3)

Starting with the nozzle thrust equation,

$$T_n = \dot{m}_n(u_{n,e} - u_{n,i}) + A_{n,e}(P_{n,e} - P_\infty) - A_{n,i}(P_{n,i} - P_\infty)$$

we recast the mass-flow rate as $A_{n,i}\rho_{n,i}u_{n,i}$ and recognize that $u_{n,i} = c_{n,i}$ and $u_{n,e} = M_{n,e}c_{n,e}$:

$$T_n = A_{n,i}\rho_{n,i}c_{n,i}(M_{n,e}c_{n,e} - c_{n,i}) + A_{n,e}(P_{n,e} - P_\infty) - A_{n,i}(P_{n,i} - P_\infty)$$

Next, factor out $A_{n,i}$:

$$T_n = A_{n,i}\left[\rho_{n,i}c_{n,i}^2\left(M_{n,e}\frac{c_{n,e}}{c_{n,i}} - 1\right) + \varepsilon(P_{n,e} - P_\infty) - (P_{n,i} - P_\infty)\right]$$

We wish to replace all densities and sound speeds by pressures. Using the isentropic relations

$$\frac{P}{P_3} = \left(\frac{\rho}{\rho_3}\right)^\gamma = \left(\frac{c}{c_3}\right)^{\frac{2\gamma}{\gamma-1}}$$

we obtain

$$T_n = A_{n,i}\left[\rho_3\left(\frac{P_{n,i}}{P_3}\right)^{\frac{1}{\gamma}}c_3^2\left(\frac{P_{n,i}}{P_3}\right)^{\frac{\gamma-1}{\gamma}}\left(M_{n,e}\left(\frac{P_{n,e}}{P_{n,i}}\right)^{\frac{\gamma-1}{2\gamma}} - 1\right) + \varepsilon(P_{n,e} - P_\infty) - (P_{n,i} - P_\infty)\right] \tag{A1}$$

Recall, from Eq. (7), the ratio of $P_{n,e}$ to $P_{n,i}$:

$$B \equiv \frac{P_{n,e}}{P_{n,i}} = (\varepsilon M_{n,e})^{-\frac{2\gamma}{\gamma+1}}$$

Next, substitute B into Eq. (A1) and eliminate ρ_3 and c_3 using P_3:

$$T_n = A_{n,i}\left[\gamma P_3\left(\frac{P_{n,i}}{P_3}\right)(M_{n,e}B^{\frac{\gamma-1}{2\gamma}} - 1) + \varepsilon(P_{n,i}B - P_\infty) - (P_{n,i} - P_\infty)\right]$$

Group the expression into a $P_{n,i}$ term and a P_∞ term:

$$T_n = A_{n,i}[P_{n,i}(\gamma(M_{n,e}B^{\frac{\gamma-1}{2\gamma}} - 1) + \varepsilon B - 1) - P_\infty(\varepsilon - 1)]$$

Eliminate B with Eq. (7) and replace $P_{n,i}$ with $P_{s,e}$:

$$T_n = A_{n,i}[P_{s,e}(\gamma M_{n,e}(\varepsilon M_{n,e})^{-\frac{\gamma-1}{\gamma+1}} - \gamma + \varepsilon(\varepsilon M_{n,e})^{-\frac{2\gamma}{\gamma+1}} - 1) - P_\infty(\varepsilon - 1)]$$

By defining G_1 and G_2,

$$G_1 \equiv \gamma M_{n,e}(\varepsilon M_{n,e})^{-\frac{\gamma-1}{\gamma+1}} + \varepsilon(\varepsilon M_{n,e})^{-\frac{2\gamma}{\gamma+1}} - \gamma - 1 \qquad G_2 \equiv \varepsilon - 1$$

we recover Eq. (3):

$$T_n = A_{n,i}(P_{s,e}G_1 - P_\infty G_2)$$

Appendix B: Deriving Equation (5)

Start with conservation of mass:

$$\frac{dm}{dt} = -\dot{m}$$

On the right side, recast the mass-flow rate as $A_s\rho_{s,e}u_{s,e}$ and recognize that $u_{s,e} = c_{s,e}$. On the left side, express m using volume and density:

$$V_s \frac{d\rho_{s,e}}{dt} = -A_s \rho_{s,e} c_{s,e}$$

Replace V_s/A_s with L_s and express all thermodynamic variables in terms of state 4:

$$L_s \rho_4 \frac{d}{dt}\left(\frac{\rho_{s,e}}{\rho_4}\right) = -\left(\frac{\rho_{s,e}}{\rho_4}\right)\left(\frac{c_{s,e}}{c_4}\right)\rho_4 c_4$$

Eliminate sound speed using the isentropic relations found in Appendix A:

$$L_s \frac{d}{dt}\left(\frac{\rho_{s,e}}{\rho_4}\right) = -\left(\frac{\rho_{s,e}}{\rho_4}\right)^{\frac{\gamma+1}{2}} c_4$$

Rearrange

$$\left(\frac{\rho_{s,e}}{\rho_4}\right)^{-\frac{\gamma+1}{2}} d\left(\frac{\rho_{s,e}}{\rho_4}\right) = -\frac{c_4}{L_s} dt$$

Because the initial density is ρ_4, we integrate $\rho_{s,e}/\rho_4$ from 1 to $\rho_{s,e}/\rho_4$ and t from t_0 to t:

$$\frac{\rho_{s,e}}{\rho_4} = \left[1 + \frac{\gamma-1}{2}\frac{c_4(t-t_0)}{L_s}\right]^{-\frac{2}{\gamma-1}}$$

Express the preceding equations as pressure using the isentropic relation to recover Eq. (5):

$$\frac{P_{s,e}}{P_4} = \left[1 + \frac{\gamma-1}{2}\frac{c_4(t-t_0)}{L_s}\right]^{-\frac{2\gamma}{\gamma-1}}$$

Appendix C: Deriving Equation (8)

For the blowdown of the nozzle, we get the impulse by integrating thrust over t_6:

$$I_n = \int_{t_0}^{t_0+t_6} T_n \mathrm{d}t$$

Using the expressions for pressure at the straight-tube exit [Eq. (5)] and nozzle thrust [Eq. (3)],

$$\frac{P_{s,e}}{P_4} = \left[1 + \frac{\gamma-1}{2}\frac{c_4(t-t_0)}{L_s}\right]^{-\frac{2\gamma}{\gamma-1}} \qquad T_n = A_{n,i}(P_{s,e}G_1 - P_\infty G_2)$$

we obtain

$$I_n = A_{n,i}\int_{t_0}^{t_0+t_6}\left(\left[1 + \frac{\gamma-1}{2}\frac{c_4(t-t_0)}{L_s}\right]^{-\frac{2\gamma}{\gamma-1}} P_4 G_1 - P_\infty G_2\right)\mathrm{d}t$$

Evaluate the integral

$$I_n = A_{n,i}\left[P_4 G_1 \frac{2}{\gamma+1}\frac{L_s}{c_4}\left(1 - \left[1 + \frac{\gamma-1}{2}\frac{c_4 t_6}{L_s}\right]^{-\frac{\gamma+1}{\gamma-1}}\right) - P_\infty G_2 t_6\right]$$

Multiply by L_s/c_3 and express P_4 using P_3:

$$I_n = \frac{A_{n,i}L_s}{c_3}\left[P_3 G_1\left(\frac{2}{\gamma+1}\right)^{\frac{2\gamma}{\gamma-1}}\frac{2}{\gamma+1}\frac{c_3}{c_4} \times \left(1 - \left[1 + \frac{\gamma-1}{2}\frac{c_4 t_6}{L_s}\right]^{-\frac{\gamma+1}{\gamma-1}}\right) - P_\infty G_2 \frac{t_6 c_3}{L_s}\right] \tag{A2}$$

Focus on the P_3 term of Eq. (A2). Define Ω_1:

$$\Omega_1 \equiv \left(\frac{2}{\gamma+1}\right)^{\frac{2\gamma}{\gamma-1}}\frac{2}{\gamma+1}\frac{c_3}{c_4}\left(1 - \left[1 + \frac{\gamma-1}{2}\frac{c_4 t_6}{L_s}\right]^{-\frac{\gamma+1}{\gamma-1}}\right)$$

Substituting the expression for t_6, Eq. (6), we obtain

$$\Omega_1 = \left(\frac{2}{\gamma+1}\right)^{\frac{2\gamma}{\gamma-1}}\frac{2}{\gamma+1}\frac{c_3}{c_4}\left(1 - \left[1 + \left(Q\frac{P_\infty}{P_3}\right)^{-\frac{\gamma-1}{2\gamma}} - 1\right]^{-\frac{\gamma+1}{\gamma-1}}\right)$$

which simplifies to

$$\Omega_1 = \left(\frac{2}{\gamma+1}\right)^{\frac{2\gamma}{\gamma-1}}\left[1 - \left(Q\frac{P_\infty}{P_3}\right)^{\frac{\gamma+1}{2\gamma}}\right]$$

which is the form of Ω_1 as it was defined in Eq. (9). Now focus on the P_∞ term of Eq. (A2) (specifically, the quantity $t_6 c_3/L_s$):

$$\frac{t_6 c_3}{L_s} = \frac{2}{\gamma-1}\frac{c_3}{c_4}\left[\left(Q\frac{P_\infty}{P_3}\right)^{-\frac{\gamma-1}{2\gamma}} - 1\right]$$

Eliminate c_3/c_4 using Eq. (1) and define the result as Ω_2:

$$\frac{t_6 c_3}{L_s} = \frac{\gamma+1}{\gamma-1}\left[\left(Q\frac{P_\infty}{P_3}\right)^{-\frac{\gamma-1}{2\gamma}} - 1\right] \equiv \Omega_2$$

Rewrite Eq. (A2) with Ω_1 and Ω_2, and replace $A_{n,i}L_s$ with V_s:

$$I_n = \frac{V_s}{c_3}(P_3 G_1 \Omega_1 - P_\infty G_2 \Omega_2)$$

which is Eq. (8), the nozzle impulse from blowdown.

Appendix D: Deriving Equation (13)

Recalling that G_1,

$$G_1 = \gamma M_{n,e}(\varepsilon M_{n,e})^{-\frac{\gamma-1}{\gamma+1}} + \varepsilon(\varepsilon M_{n,e})^{-\frac{2\gamma}{\gamma+1}} - \gamma - 1$$

we write this in terms of B using Eq. (7):

$$G_1 = \gamma M_{n,e} B^{\frac{\gamma-1}{2\gamma}} + \varepsilon B - \gamma - 1$$

Differentiate

$$G_1' = \gamma B^{\frac{\gamma-1}{2\gamma}} + \frac{\gamma-1}{2} M_{n,e} B^{-\frac{\gamma+1}{2\gamma}} B' + \varepsilon' B + \varepsilon B'$$

Divide by G_2', which is equal to ε':

$$\frac{G_1'}{G_2'} = \gamma\frac{B^{\frac{\gamma-1}{2\gamma}}}{\varepsilon'} + \frac{\gamma-1}{2} M_{n,e}\frac{B^{-\frac{\gamma+1}{2\gamma}}B'}{\varepsilon'} + B + \frac{\varepsilon}{\varepsilon'}B' \tag{A3}$$

From Eq. (7) it is straightforward to show

$$B' = -\frac{2\gamma}{\gamma+1} M_{n,e} B^{\frac{2\gamma-1}{\gamma}} \tag{A4}$$

Substitute Eq. (A4) into Eq. (A3):

$$\frac{G_1'}{G_2'} = \gamma\frac{B^{\frac{\gamma-1}{2\gamma}}}{\varepsilon'} - \gamma\frac{\gamma-1}{\gamma+1} M_{n,e}^2\frac{B^{\frac{3\gamma-3}{2\gamma}}}{\varepsilon'} + B - \frac{2\gamma}{\gamma+1}\frac{\varepsilon}{\varepsilon'} M_{n,e} B^{\frac{2\gamma-1}{\gamma}}$$

Factor common terms

$$\frac{G_1'}{G_2'} = B + \gamma\frac{B^{\frac{\gamma-1}{2\gamma}}}{\varepsilon'}\left[1 - \frac{\gamma-1}{\gamma+1} M_{n,e}^2 B^{\frac{\gamma-1}{\gamma}} - \frac{2}{\gamma+1}\varepsilon M_{n,e} B^{\frac{3\gamma-1}{2\gamma}}\right]$$

Factor further

$$\frac{G_1'}{G_2'} = B + \gamma\frac{B^{\frac{\gamma-1}{2\gamma}}}{\varepsilon'}\left[1 - \frac{2}{\gamma+1} B^{\frac{\gamma-1}{\gamma}}\left(\frac{\gamma-1}{2} M_{n,e}^2 + \varepsilon M_{n,e} B^{\frac{\gamma+1}{2\gamma}}\right)\right]$$

The last term is unity:

$$\frac{G_1'}{G_2'} = B + \gamma\frac{B^{\frac{\gamma-1}{2\gamma}}}{\varepsilon'}\left[1 - \frac{2}{\gamma+1} B^{\frac{\gamma-1}{\gamma}}\left(\frac{\gamma-1}{2} M_{n,e}^2 + 1\right)\right]$$

Using Eq. (7), write the B that appears inside the brackets in terms of $M_{n,e}$:

$$\frac{G_1'}{G_2'} = B + \gamma \frac{B^{\frac{\gamma-1}{2\gamma}}}{\varepsilon'} \times \left[1 - \frac{2}{\gamma+1}\left(\frac{1+[(\gamma-1)/2M_{n,e}^2}{[(\gamma+1)/2}\right)^{-1}\left(\frac{\gamma-1}{2}M_{n,e}^2 + 1\right)\right]$$

Rearrange

$$\frac{G_1'}{G_2'} = B + \gamma \frac{B^{\frac{\gamma-1}{2\gamma}}}{\varepsilon'} \times \left[1 - \left(\frac{1+[(\gamma-1)/2]M_{n,e}^2}{(\gamma+1)/2}\right)^{-1}\left(\frac{1+[(\gamma-1)/2M_{n,e}^2}{(\gamma+1)/2}\right)\right] = B$$

Eliminating B using Eq. (7), we recover Eq. (13):

$$\frac{G_1'}{G_2'} = (\varepsilon M_{n,e})^{-\frac{2\gamma}{\gamma+1}}$$

Acknowledgment

This work was supported by the Office of Naval Research, with Gabriel Roy serving as technical monitor.

References

[1] Roy, G. D., Frolov, S. M., Borisov, A. A., and Netzer, D. W., "Pulse Detonation Propulsion: Challenges, Current Status, and Future Perspective," *Progress in Energy and Combustion Science*, Vol. 30, No. 6, 2004, pp. 545–672. doi:10.1016/j.pecs.2004.05.001

[2] Cooper, M., Shepherd, J. E., and Schauer, F., "Impulse Correlation for Partially Filled Detonation Tubes," *Journal of Propulsion and Power*, Vol. 20, No. 5, 2004, pp. 947–950. doi:10.2514/1.4997

[3] Kailasanath, K., "A Review of Research on Pulse Detonation Engine Nozzles," 37th AIAA/ASME/SAE/ASEE Joint Propulsion Conference, Salt Lake City, UT, AIAA Paper 2001-3932, 2001.

[4] Cambier, J.-L., and Tegnér, J. K., "Strategies for Pulsed Detonation Engine Performance Optimization," *Journal of Propulsion and Power*, Vol. 14, No. 4, 1998, pp. 489–498. doi:10.2514/2.5305

[5] Eidelman, S., and Yang, X., "Analysis of the Pulse Detonation Engine Efficiency," 34th AIAA/ASME/SAE/ASEE Joint Propulsion Conference, Cleveland, OH, AIAA Paper 1998-3877, 1998.

[6] Morris, C. I., "Numerical Modeling of Single-Pulse Gasdynamics and Performance of Pulse Detonation Rocket Engines," *Journal of Propulsion and Power*, Vol. 21, No. 3, 2005, pp. 527–538. doi:10.2514/1.7875

[7] Owens, Z. C., and Hanson, R. K., "Single-Cycle Unsteady Nozzle Phenomena in Pulse Detonation Engines," *Journal of Propulsion and Power*, Vol. 23, No. 2, 2007, pp. 325–337. doi:10.2514/1.22415

[8] Cooper, M., and Shepherd, J. E., "Single-Cycle Impulse from Detonation Tubes with Nozzles," *Journal of Propulsion and Power*, Vol. 24, No. 1, 2008, pp. 81–87. doi:10.2514/1.30192

[9] Morris, C. I., "Axisymmetric Modeling of Pulse Detonation Rocket Engines," *41st AIAA/ASME/SAE/ASEE Joint Propulsion Conference*, Tucson, AZ, AIAA Paper 2005-3508, 2005.

[10] Wintenberger, E., Austin, J. M., Cooper, M., Jackson, S., Shepherd, J. E., "Analytical Model for the Impulse of Single-Cycle Pulse Detonation Tube," *Journal of Propulsion and Power*, Vol. 19, No. 1, 2003, pp. 22–38. doi:10.2514/2.6099

[11] Cooper, M., and Shepherd, J. E., "Detonation Tube Impulse in Subatmospheric Environments," *Journal of Propulsion and Power*, Vol. 22, No. 4, 2006, pp. 845–851. doi:10.2514/1.16979

[12] Kiyanda, C. B., Tanguay, V., Higgins, A. J., "Effect of Transient Gasdynamic Processes on the Impulse of Pulse Detonation Engines," *Journal of Propulsion and Power*, Vol. 18, No. 5, 2002, pp. 1124–1126. doi:10.2514/2.6045

[13] Radulescu, M. I., and Hanson, R. K., "Comment on 'Analytical Model for the Impulse of Single-Cycle Pulse Detonation Tube,'" *Journal of Propulsion and Power*, Vol. 20, No. 5, 2004, pp. 956–957. doi:10.2514/1.7876

[14] Reynolds, W. C., "STANJAN: Interactive Computer Program for Chemical Equilibrium Analysis," Department of Mechanical Engineering, Stanford Univ.,, TR SUMET-8108, Stanford, CA, Jan. 1986.

[15] Wintenberger, E. "Application of Steady and Unsteady Detonation Waves to Propulsion," Ph.D. Dissertation, California Inst. of Technology, Pasadena, CA, 2004, Sec. 1.1.4.

[16] Rudinger, G., *Nonsteady Duct Flow: Wave-Diagram Analysis*, Dover, New York, 1969, pp. 186–198.

[17] Thompson, P. A., *Compressible-Fluid Dynamics*, McGraw–Hill, New York, 1972, p. 175.

[18] Anderson, J. D. Jr., *Modern Compressible Flow with Historical Perspective*, McGraw–Hill, New York, 1982, p. 179.

[19] Barbour, E. A., Hanson, R. K., Morris, C. I., Radulescu, M. I., "A Pulsed Detonation Tube with a Converging-Diverging Nozzle Operating at Different Pressure Ratios," 43rd AIAA Aerospace Sciences Meeting, Reno, NV, AIAA Paper 2005-1307, 2005.

[20] Radulescu, M. I., Hanson, R. K., "Effect of Heat Loss on Pulse-Detonation-Engine Flow Fields and Performance," *Journal of Propulsion and Power*, Vol. 21, No. 2, 2005, pp. 274–285. doi:10.2514/1.10286

[21] Sutton, G. P., *Rocket Propulsion Elements*, 6th ed., Wiley, New York, 1992, pp. 41–68.

[22] Zukas, J. A., and Walters, W. P., *Explosive Effects and Applications*, Springer, New York, 1998, Chap. 7.

[23] Cooper, M., "Impulse Generated by Detonation Tubes," Ph.D. Dissertation, California Inst. of Technology, Pasadena, CA, 2004, Sec. 3.3.3.

J. Powers
Associate Editor